



Study of immiscible displacements in porous media using a color-gradient-based multiphase lattice Boltzmann method



Haibo Huang^{a,*}, Jun-Jie Huang^b, Xi-Yun Lu^a

^a Dept. of Modern Mechanics, Univ. of Sci. and Tech. of China, Hefei 230026, China

^b Dept. of Engineering Mechanics, Chongqing University, Chongqing 400044, China

ARTICLE INFO

Article history:

Received 12 September 2013

Received in revised form 13 January 2014

Accepted 18 January 2014

Available online 6 February 2014

Keywords:

Lattice Boltzmann

Multiphase

Color-gradient

Rothman–Keller

Multi-component

Porous media

ABSTRACT

A multiple-relaxation-time (MRT) Rothman and Keller (R–K) lattice Boltzmann model is presented for two phase flows with kinematic viscosity contrast. For two-phase flows in porous media, the numerical stability may be reduced due to the presence of complex wall boundaries. The MRT R–K model is shown to be able to ensure better numerical stability and reduce spurious currents significantly. The non-equilibrium bounce back scheme is extended to handle the pressure and velocity boundary condition in two-phase flow simulations. Immiscible displacement in complex heterogeneous media is investigated and three typical flow patterns are obtained, stable displacement, viscous fingering and capillary fingering. Cases with both capillary number Ca and viscosity ratio M ranging from 10^{-3} to 10^3 are simulated. The three typical flow patterns correspond to the three domains in the M – Ca phase-diagram. The boundaries that separate the three domains in the model results are qualitatively consistent with previous experimental studies. The MRT R–K model coupled with the developed boundary condition is a good tool for the study of two-phase flows in porous media.

© 2014 Elsevier Ltd. All rights reserved.

1. Introduction

Numerous macroscopic numerical methods have been developed for solving the two-phase Navier–Stokes (N–S) equations [1], such as the front-tracking method, volume-of-fluid (VOF) method, level set method, and so on. The former three methods are the most popular ones. However, the front-tracking method is usually not able to simulate interface coalescence or break-up [1,2]. In the VOF and level set methods, usually the interface reconstruction step or interface reinitialization is required, which may be non-physical or complex to implement [2]. Besides, numerical instability may appear when the VOF and level set methods are applied to simulate surface-tension-dominated flows in complex geometries [1].

In the last twenty years, the Lattice Boltzmann method (LBM) has been developed into a good tool to solve two-phase flow in porous media [3–8]. The LBM is a mesoscopic method and easily handles complex wall geometries. It is also an explicit method, which makes the code easy to parallelize. In the LBM, solving the Poisson equation is not required, hence it is more efficient than common macroscopic schemes.

There are many multiphase LBMs available in the literature, such as the Shan–Chen model [9], free energy model [10], Rothman–Keller model [11], and so on. The Shan–Chen multiphase model is the simplest one [4]. However, quantitative numerical study shows the existing model is not accurate [12] due to the inaccurate forcing term used in the model [13].

The first multi-component lattice gas model was proposed by Rothman and Keller [11]. The model was further developed by Gunstensen et al. [14] and an extra binary fluid collision was introduced into the Lattice Boltzmann equation. Latva-Kokko and Rothman [15] improved the recoloring step in the R–K model, reduced the lattice pinning effect and decreased the spurious currents [2,16]. Now that recoloring step is widely used in applications of the R–K model [2,12,17]. Recently, Reis and Phillips developed a two-dimensional nine-velocity R–K model [18]. In the model, a revised binary fluid collision is proposed and is shown to be able to recover the additional term which accounts for surface tension in the N–S equations [18].

Swift et al. analyzed the possible similarity between the free energy model and the R–K model [10]. However, the recoloring step in the R–K model prevented further theoretical comparative analysis between the two models. Numerical study shows that the numerical accuracy and efficiency of the free energy model and the R–K model are comparable [12], which suggests some potential similarity between the models.

* Corresponding author. Tel.: +86 0551 3603345.

E-mail address: huanghb@ustc.edu.cn (H. Huang).

On the other hand, the ways of imposing wetting boundary conditions for the two models are very different [12]. For the free-energy model, the gradient of the density near the wall should be imposed and the normal derivative has to be calculated. To apply the condition, the densities of the surrounding lattice nodes near the wall are involved [19]. For example, using the free-energy model, Liu et al. achieved density ratio as high as $O(100)$ in their simulations [19], and they identified three typical flow patterns in the immiscible displacements in porous media. However, in their simulations, to get the surface normal derivative in an arbitrary inclined direction is not easy and hence, only simple squares are used to represent the solid grains [19].

For the R–K model, specifying the wetting condition is much simpler because only the densities of the two fluids in the solid nodes should be specified. Due to this simplicity, the R–K model has advantages over the free-energy model for two-phase flows in porous media. Hence, this model has been applied to simulations of multiphase flows in porous media [5,20]. However, most previous LBM studies are confined to only a narrow range of parameters [5,20,21]; for example, the maximum viscosity ratio in Ref. [5] is approximately 10.

Later, by introducing two free parameters in the rest equilibrium distribution function (DF), Grunau et al. [22] claimed the improved R–K model was able to simulate flows with different densities. However, it has been proved theoretically and numerically that this is not true for general two-phase flows [23,24]. The improvement proposed by Huang et al. [24] for the model is valid for cases with lower density ratios. Here, we focus on the model with identical densities but different viscosities.

Applying a more sophisticated finite difference method could make the color gradient more isotropic and eliminate the spurious currents around the bubble or droplet [25]. However, the more sophisticated finite difference has to include many surrounding points. For example, usually the color gradient can be obtained from the information on the surrounding 8 points in 2D simulations when the D2Q9 velocity model is used. However, the sophisticated finite difference requires information of the surrounding 25 points. Hence, it is not convenient to perform this sophisticated finite difference on the simulations of flow in porous media because the densities of the solid nodes inside the first layer of the wall, which may be used in the computation, are not specified and unknown.

As we know, reducing spurious currents is an important issue for multiphase models. In almost all of the lattice Boltzmann multiphase models, when surface tension increases, the magnitude of spurious current would increase to some extent [12,13]. In simulations of two phase flows with low capillary number ($Ca = \frac{\mu u}{\sigma}$, where μ , u , σ are fluid dynamic viscosity, characteristic flow velocity, and surface tension, respectively) in porous media, a large surface tension coupled with small spurious currents is preferred, otherwise the spurious current would affect the main flow (velocity is small) in the pore space.

It is also noted in the study of Liu et al. [19], the kinematic viscosity ratio of liquid and gas is kept unity and the dynamic viscosity ratio is equal to the density ratio. The minimum viscosity ratio seems limited to 10^{-2} . Here in the R–K method, the multiple-relaxation-time (MRT) collision model [26] is adopted. The present method is able to reduce spurious currents and improve numerical stability significantly. The multiphase flows with viscosity ratios ranging from 10^{-3} to 10^3 can be simulated. Those are good ranges for reproducing the capillary fingering phenomena for two phase flows in porous media. That will be discussed in Section 5 in detail.

The paper is arranged in the following way. First the present MRT R–K model is introduced. Then the properties of surface tension calculation, isotropy, spurious currents, and contact angle of this model are investigated. The MRT R–K LBM is shown to be more

stable and able to reduce the spurious current further than the BGK model. Two dynamic multiphase flow problems are simulated to validate our numerical method. Finally, displacements in porous media with capillary numbers and viscosity ratios ranging from 10^{-3} to 10^3 are simulated. The simulated flow patterns are consistent with experimental studies [27].

2. Method

2.1. R–K model

In the R–K model, the particle distribution function (PDF) for fluid k is defined to be f_i^k . For two-phase flows, two distribution functions are defined, i.e., f_i^b , and f_i^r , where b and r denote ‘blue’ or ‘red’ component. The total PDF at (\mathbf{x}, t) is $f_i(\mathbf{x}, t) = \sum_k f_i^k(\mathbf{x}, t)$.

Usually there are two steps implemented in the LBM, collision and streaming. In the R–K model, there are three steps for each component: streaming, collision, and recoloring. Suppose an iteration begins from the streaming step. We illustrate how the three steps construct a loop. The streaming step is [18]

$$f_i^k(\mathbf{x} + \mathbf{e}_i \delta t, t + \delta t) = f_i^{k+}(\mathbf{x}, t), \tag{1}$$

where f_i^{k+} is the PDF after the recoloring step. In the above equation, \mathbf{e}_i , $i = 0, 1, \dots, b$ are the discrete velocities of the velocity models. For the D2Q9 velocity model ($b = 8$), $\frac{e_{ix}}{c}$, $\frac{e_{iy}}{c}$ are illustrated in the 4th and 6th row vectors, respectively in Appendix. Here c is the lattice speed defined to be $c = \frac{\delta x}{\delta t}$. We use the lattice units of 1 l.u. = $1\delta x$, 1 t.s. = $1\delta t$, and the mass unit is m.u. in our study.

The collision step can be written as [15]

$$f_i^{k*}(\mathbf{x}, t) = f_i^k(\mathbf{x}, t) + (\Omega_i^k)^1 + (\Omega_i^k)^2, \tag{2}$$

where $f_i^{k*}(\mathbf{x}, t)$ is the post-collision state. There are two collision terms in the equation, i.e., $(\Omega_i^k)^1$ and $(\Omega_i^k)^2$. If the lattice BGK scheme is adopted, the first collision term is

$$(\Omega_i^k)^1 = -\frac{\delta t}{\tau} \left(f_i^k(\mathbf{x}, t) - f_i^{k,eq}(\mathbf{x}, t) \right), \tag{3}$$

where τ is the relaxation time.

The equilibrium distribution function $f_i^{k,eq}(\mathbf{x}, t)$ can be calculated using [18]

$$f_i^{k,eq}(\mathbf{x}, t) = \rho_k \left(C_i + w_i \left[\frac{\mathbf{e}_i \cdot \mathbf{u}}{c_s^2} + \frac{(\mathbf{e}_i \cdot \mathbf{u})^2}{2c_s^4} - \frac{(\mathbf{u})^2}{2c_s^2} \right] \right), \tag{4}$$

where the density of the k th component is

$$\rho_k = \sum_i f_i^k, \tag{5}$$

and the total density is $\rho = \sum_k \rho_k$. The momentum is

$$\rho \mathbf{u} = \sum_k \sum_i f_i^k \mathbf{e}_i. \tag{6}$$

In the above formula, the coefficients are [18] $C_0 = \alpha_k$, $C_i = \frac{1-2\alpha_k}{5}$, $i = 1, 2, 3, 4$ and $C_i = \frac{1-2\alpha_k}{20}$, $i = 5, 6, 7, 8$, where α_k is a parameter that is assumed able to adjust the density of fluids [18,22] but this is not true [24]. The other parameters are $w_0 = \frac{4}{9}$, $w_i = \frac{1}{9}$, $i = 1, 2, 3, 4$, and $w_i = \frac{1}{36}$, $i = 5, 6, 7, 8$.

When the relaxation time parameters for the two fluids are very different, for example, $\tau_r = 0.501$ and $\tau_b = 1.0$, $\tau(\mathbf{x})$ at the interface can be determined by a simple way: $\psi(\mathbf{x}) = \frac{\rho_r(\mathbf{x}) - \rho_b(\mathbf{x})}{\rho_r(\mathbf{x}) + \rho_b(\mathbf{x})} > 0$, $\tau(\mathbf{x}) = \tau_r$ and otherwise $\tau(\mathbf{x}) = \tau_b$. To make the relaxation parameter ($\tau(\mathbf{x})$) change smoothly at the interfaces between two fluids, here we adopt the interpolation scheme constructed by Grunau et al. [18,22].

$$\tau = \begin{cases} \tau_r & \psi > \delta, \\ g_r(\psi) & \delta \geq \psi > 0, \\ g_r(\psi) & 0 \geq \psi \geq -\delta, \\ \tau_b & \psi < -\delta, \end{cases}$$

where $g_r(\psi) = s_1 + s_2\psi + s_3\psi^2$, $g_b(\psi) = t_1 + t_2\psi + t_3\psi^2$, and $s_1 = t_1 = 2 \frac{\tau_r \tau_b}{\tau_r + \tau_b}$, $s_2 = 2 \frac{\tau_r - \alpha}{\delta}$, $s_3 = -\frac{\beta}{2\delta}$, $t_2 = 2 \frac{\alpha - \tau_b}{\delta}$, and $t_3 = \frac{\beta}{2\delta}$. Here $\delta \leq 1$ is a free positive parameter. The viscosity of each component is $\nu_k = c_s^2(\tau_k - 0.5)$, where $c_s^2 = \frac{1}{3}c^2$. The viscosity ratio is defined as $M = \frac{\nu_{nw}}{\nu_w}$, where the subscript “nw”, “w” denote the non-wetting fluid and wetting fluid, respectively.

The second collision term is more complex and there are some different forms found in the literature [8,18]. An example is [8]:

$$(\Omega_i^k)^2 = \frac{A}{2} |\mathbf{f}| (2 \cdot \cos^2(\lambda_i) - 1), \quad (7)$$

where λ_i is the angle between the color gradient \mathbf{f} and the direction \mathbf{e}_i , and we have $\cos(\lambda_i) = \frac{\mathbf{e}_i \cdot \mathbf{f}}{|\mathbf{e}_i| |\mathbf{f}|}$ [15].

The color-gradient $\mathbf{f}(\mathbf{x}, t)$ is calculated as [15]:

$$\mathbf{f}(\mathbf{x}, t) = \sum_i \mathbf{e}_i \sum_j [f_j^r(\mathbf{x} + \mathbf{e}_i \delta t, t) - f_j^b(\mathbf{x} + \mathbf{e}_i \delta t, t)]. \quad (8)$$

However, according to the study of Reis and Phillips [18], the correct collision operator should be

$$(\Omega_i^k)^2 = \frac{A}{2} |\mathbf{f}| \left[w_i \frac{(\mathbf{e}_i \cdot \mathbf{f})^2}{|\mathbf{f}|^2} - B_i \right], \quad (9)$$

where $B_0 = -\frac{4}{27}$, $B_i = \frac{2}{27}$, $i = 1, 2, 3, 4$, $B_i = \frac{5}{108}$, $i = 5, 6, 7, 8$. Using these parameters, the correct term due to surface tension in the N–S equations can be recovered [18].

Then the recoloring step is implemented to achieve separation of the two fluids [15],

$$f_i^{r,+} = \frac{\rho_r}{\rho} f_i^* + \beta \frac{\rho_r \rho_b}{\rho^2} f_i^{(eq)}(\rho, 0) \cos(\lambda_i), \quad (10)$$

$$f_i^{b,+} = \frac{\rho_b}{\rho} f_i^* - \beta \frac{\rho_r \rho_b}{\rho^2} f_i^{(eq)}(\rho, 0) \cos(\lambda_i), \quad (11)$$

where $f_i^* = \sum_k f_i^{k*}$.

After $f_i^r(\mathbf{x}, t)$, and $f_i^b(\mathbf{x}, t)$ are updated, the streaming steps (i.e., Eq. (1)) should be implemented for each component. Through iteration of the procedure illustrated above, two-phase flows can be simulated.

In the model, A , and β are the two most important parameters that adjust interfacial properties. The interfacial thickness can be adjusted by β but the surface tension is independent of β and only determined by A and τ_r , τ_b [15]. The pressure in the flow field can be obtained from the density via the equation of state $p = c_s^2 \rho$.

In our study, only components with identical densities are considered and the corresponding equilibrium DF is Eq. (4) with $C_i = w_i$. That is the common equilibrium DF usually used in the LBM [28]. Hence, for two components with identical densities, the equilibrium DF has the same formula. It is not necessary to calculate both collision step Eqs. (3) and (9) separately for each component. The two collision steps become,

$$(\Omega_i)^1 = -\frac{\delta t}{\tau} (f_i(\mathbf{x}, t) - f_i^{(eq)}(\mathbf{x}, t)), \quad (12)$$

and

$$(\Omega_i)^2 = A |\mathbf{f}| \left[w_i \frac{(\mathbf{e}_i \cdot \mathbf{f})^2}{|\mathbf{f}|^2} - B_i \right], \quad (13)$$

where $f_i = \sum_k f_i^k$.

2.2. MRT R–K model

The difference between the MRT and BGK R–K model is the collision term. The collision term $(\Omega_i)^1$ in Eq. (12) should be replaced by the MRT collision model [26]. That is,

$$(\Omega_i)^1 = -M^{-1} \widehat{\mathbf{S}} [|m(\mathbf{x}, t)\rangle - |m^{(eq)}(\mathbf{x}, t)\rangle], \quad (14)$$

where the Dirac notation of ket $|\cdot\rangle$ vectors symbolize column vectors. The collision matrix $\widehat{\mathbf{S}} = M \cdot S \cdot M^{-1}$ is diagonal with $\widehat{\mathbf{S}} = \text{diag}(s_0, s_1, \dots, s_b)$. $|m^{(eq)}\rangle$ is the equilibrium value of the moment $|m\rangle$. The matrix M illustrated in the Appendix is a linear transformation which is used to map a vector $|f\rangle$ in discrete velocity space to a vector $|m\rangle$ in moment space, i.e., $|m\rangle = M \cdot |f\rangle$, $|f\rangle = M^{-1} \cdot |m\rangle$.

The momenta $j_\zeta = \rho u_\zeta$ are obtained from

$$j_\zeta = \sum_i f_i e_{i\zeta}, \quad (15)$$

where ζ denotes x or y coordinates. The collision process is executed in moment space [26]. For the D2Q9 model, $|m\rangle = (\rho, e, \epsilon, j_x, q_x, j_y, q_y, p_{xx}, p_{xy})^T$, where e , ϵ , and q_ζ are the energy, the energy square, and the heat flux, respectively. $|m^{(eq)}\rangle = (\rho, e^{eq}, \epsilon^{eq}, j_x^{eq}, q_x^{eq}, j_y^{eq}, q_y^{eq}, p_{xx}^{eq}, p_{xy}^{eq})^T$, where $e^{eq} = -2\rho + 3(j_x^2 + j_y^2)/\rho$, $\epsilon^{eq} = \rho - 3(j_x^2 + j_y^2)/\rho$, $q_x^{eq} = -j_x$, $q_y^{eq} = -j_y$, $p_{xx}^{eq} = (j_x^2 - j_y^2)/\rho$, $p_{xy}^{eq} = j_x j_y / \rho$. The diagonal collision matrix $\widehat{\mathbf{S}}$ is given by [26].

$\widehat{\mathbf{S}} \equiv \text{diag}(s_0, s_1, s_2, s_3, s_4, s_5, s_6, s_7, s_8)$. The parameters are chosen as: $s_0 = s_3 = s_5 = 1.0$, $s_1 = 1.64$, $s_2 = 1.54$, $s_4 = s_6 = 1.2$, and $s_7 = s_8 = \frac{1}{2}$.

2.3. Boundary conditions

To simulate immiscible displacements, the velocity inlet boundary condition and constant pressure (or density) boundary conditions are set for the upper and lower boundary, respectively. In our simulations, only non-wetting fluid displacing wetting fluid is considered.

In the upper boundary the DF f_4 , f_7 , f_8 are unknown after the streaming step for the non-wetting fluid (majority component). Through non-equilibrium bounce back assumption [29], one gets the density of the majority component is

$$\rho_n = \frac{f_0^n + f_1^n + f_3^n + 2(f_2^n + f_5^n + f_6^n)}{1 + u_i}, \quad (16)$$

and the unknowns can be obtained through [29]

$$\begin{aligned} f_4^n &= f_2^n - \frac{2}{3} \rho_n u_i, \\ f_7^n &= f_5^n + \frac{1}{2} (f_1^n - f_3^n) - \frac{1}{6} \rho_n u_i, \\ f_8^n &= f_6^n + \frac{1}{2} (f_3^n - f_1^n) - \frac{1}{6} \rho_n u_i, \end{aligned} \quad (17)$$

where u_i is the specified inlet velocity of the non-wetting fluid.

The pressure boundary conditions for the lower boundary can be handled similarly [29]. Suppose ρ_s is the density of the wetting component (majority component) that is specified on the lower outlet boundary node. One can get the outlet velocity of wetting fluid

$$u_y = 1 - \frac{f_0^w + f_1^w + f_3^w + 2(f_4^w + f_7^w + f_8^w)}{\rho_s}, \quad (18)$$

and the unknowns are

$$\begin{aligned}
 f_2^w &= f_4^w + \frac{2}{3} \rho_s u_y, \\
 f_5^w &= f_7^w + \frac{1}{2} (f_3^w - f_1^w) + \frac{1}{6} \rho_s u_y, \\
 f_6^w &= f_8^w + \frac{1}{2} (f_1^w - f_3^w) + \frac{1}{6} \rho_s u_y.
 \end{aligned}
 \tag{19}$$

We note that maintaining the density (or pressure) of the minority component, which is usually set to be a very small value, say 10^{-8} m.u./l.u.³, on both the upper and lower boundaries is also important.

3. Surface tension, isotropy, contact angle and spurious currents

3.1. Surface tension

In the Sections 3.1 and 3.2, the cases of a droplet immersed in another fluid are simulated.

The surface tension σ as a function of A for the R–K simulations with viscosity ratio $M = 1$ can be determined analytically [18]. However, how to analytically determine the surface tension for $M \neq 1$ is an open question. Here σ is determined through numerical simulations of a droplet using the Laplace law. σ as a function of A for different M is illustrated in Table 1. Here we can see that over a wide range, if M is fixed, $\frac{\sigma}{A}$ is almost a constant, which means σ changes linearly with the parameter A .

3.2. Isotropy

In the study of Hou et al. [30], the isotropy of R–K model was investigated. However, in their work the “recolor” step utilized an outdated approach [11,14] and the parameters in their study [30] are fixed to a narrow range. Because the combination of the MRT and “recolor” step proposed by Latva-Kokko and Rothman

Table 1
Surface tension as a function of A for different viscosity ratios (MRT R–K model).

A	τ_r	τ_b	$\frac{\sigma}{A}$
$10^{-6} \sim 10^{-2}$	1.0	1.0	2.69
$10^{-6} \sim 10^{-2}$	1.5	0.55	2.79
$10^{-6} \sim 10^{-2}$	1.5	0.51	2.72
$10^{-6} \sim 10^{-2}$	1.5	0.502	2.74
$10^{-6} \sim 10^{-2}$	1.0	0.505	2.05
$10^{-6} \sim 10^{-2}$	1.0	0.501	1.96
$10^{-6} \sim 10^{-2}$	0.501	1.0	1.96

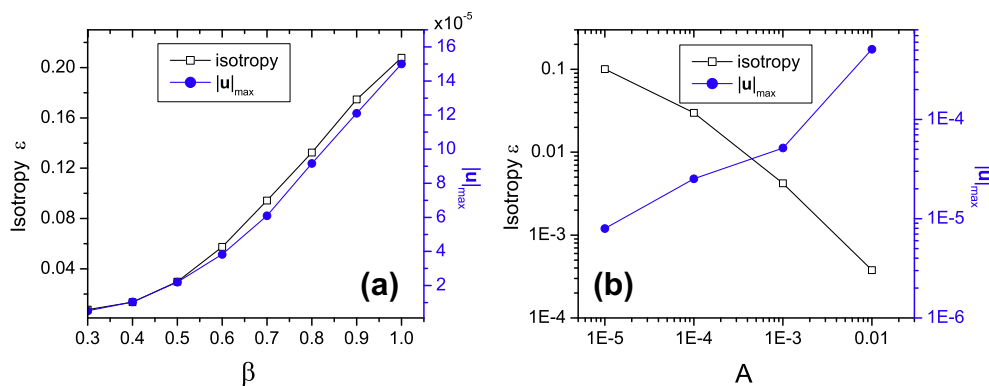


Fig. 1. (a) Isotropy and the magnitude of maximum spurious current as functions of β with $A = 10^{-4}$. (b) Isotropy and the magnitude of maximum spurious current as functions of A with $\beta = 0.5$.

[15], which is developed here has never been applied to isotropy, it is necessary to re-evaluate the isotropy.

Fig. 1 shows the isotropy which is defined as $\epsilon = \frac{r_{max} - r_{min}}{r_{min}}$ and the magnitude of the maximum spurious current $|u|_{max}$ as functions of β when $A = 10^{-4}$. r_{max} and r_{min} are the maximum and minimum radii in eight directions, which are consistent with the vectors e_i , $i = 1, \dots, 8$. We can see that both ϵ and $|u|_{max}$ increase with β . However, smaller β is not a good choice because when β is small, the interface becomes thick. For example, the interfacial thicknesses are approximately 7 l.u., 5 l.u., 4 l.u., and 3 l.u. for $\beta = 0.3, 0.4, 0.5$, and 0.7 , respectively. Thick interfaces are not desirable in simulations of two-phase flow in porous media. Usually $\beta = 0.5$ or 0.4 is used in our simulations. Note that β does not change the surface tension but affects the interface thickness, isotropy, and the magnitude of spurious current.

Note that in Table 1, when A is small, for example, $A = 10^{-5}$, the isotropy of the droplet may be not good if $\beta = 0.5$; using smaller β is helpful to achieve better isotropy of the droplet.

3.3. Contact angle

Using the MRT R–K model, wetting phenomena are simulated. In our 2D simulations, the computational domain is 200×100 , the top and bottom of the domain are bounded by two walls and periodic boundary conditions are applied on the left and right boundaries. It is noted that both the densities of the majority and minority components should be specified at each lattice node inside the computational domain. In our simulations, a circle with radius $r = 25$ l.u. just above the bottom wall is initialized as red fluid (the majority component $\rho_r = \rho_i$ and the minority component $\rho_b = 0$) and the remaining area is initialized as blue fluid (the minority component $\rho_r = 0$ and the majority component $\rho_b = \rho_i$), where $\rho_i = 1.0$ m.u./l.u.³ is an initial density.

The contact angles obtained from the present MRT R–K model are illustrated in Fig. 2. Through setting ρ_r and ρ_b values on the wall nodes, i.e., ρ_{wr} and ρ_{wb} , different contact angles can be obtained. The simulated angles can be measured via the scheme in Ref. [28], for example.

In Fig. 2, the spurious currents are also shown. The maximum magnitudes of the current are also given in the caption. In this figure, we can also see there are small circular flow patterns near the three-phase contact point, which may be induced by the uncompensated stress at that point [17].

The contact angle θ can be analytically determined by [15]

$$\theta = \arccos\left(\frac{\rho_{wr} - \rho_{wb}}{\rho_i}\right),
 \tag{20}$$

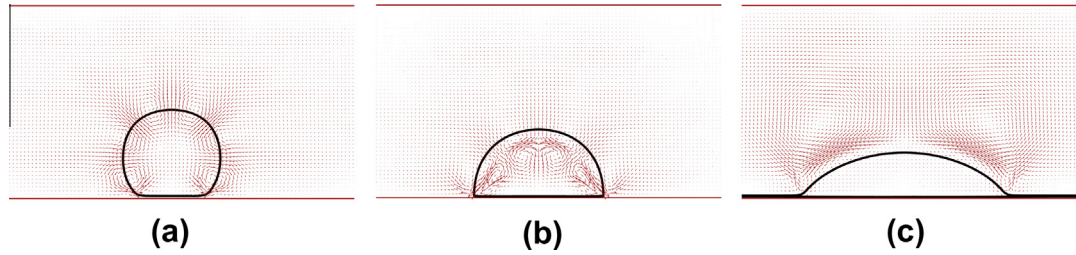


Fig. 2. Contact angles and the equilibrium spurious current for present MRT R-K model. (a) $\rho_{wr} = -0.7$, $\rho_{wb} = 0.0$, $\tau_r = 1$, $\tau_b = 0.6$, $|\mathbf{u}|_{\max} = 6.77 \times 10^{-5}$, (b) $\rho_{wr} = \rho_{wb} = 0.0$, $\tau_r = 0.501$, $\tau_b = 1$, $|\mathbf{u}|_{\max} = 9.97 \times 10^{-5}$, (c) $\rho_{wr} = 0.7$, $\rho_{wb} = 0.0$, $\tau_r = 1$, $\tau_b = 0.501$, $|\mathbf{u}|_{\max} = 2.09 \times 10^{-4}$.

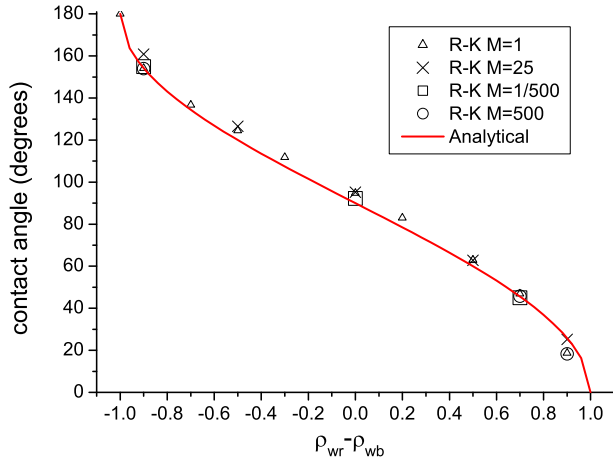


Fig. 3. Contact angles obtained from present MRT R-K model compared with the analytical solution. Viscosity ratios $M = 1$, $M = 25$, $M = \frac{1}{500}$, and $M = 500$ are simulated.

where θ is measured from the red component. From the above equation, we can see that the difference between ρ_{wr} and ρ_{wb} determines the wetting property. The possible reason is that ρ_{wr} and ρ_{wb} affect the wetting property of the wall through the color gradient illustrated in Eq. (8).

In Fig. 3, the simulated angles are compared with Eq. (20). From the figure, we can see that for $M = 1$, 25, $\frac{1}{500}$, 500, the contact angles obtained from present MRT R-K model agree well with those obtained from Eq. (20). Hence, the validity of Eq. (20) is independent of the viscosity contrast.

3.4. Spurious currents

The spurious currents in the simulations are investigated so as to compare the performance of the MRT and BGK models. The simulations of different contact angles with various viscosity ratios were carried out. The magnitudes of the spurious current are shown in Table 2. We can see that when $M = 0.002$ or $M = 500$, the spurious current (MRT) is approximately one order of magnitude less than that obtained from the BGK model. Hence, compared to the BGK R-K model, the MRT R-K model decreases the spurious current significantly at high viscosity contrast.

4. Further numerical validation

In this section, two dynamic multiphase flows are simulated to validate our numerical method. One case is the injection of a non-wetting gas into two parallel capillary tubes [19]. The other is the capillary filling dynamic [31], i.e., liquid filling a capillary tube that initially contains gas. Here the component with smaller dynamic

Table 2

Spurious current in the MRT and BGK R-K simulations (cases of contact angle with different viscosity ratios ($A = 10^{-4}$, $\beta = 0.5$)).

BGK or MRT	τ_r	τ_b	$\rho_{wr} - \rho_{wb}$	$ \mathbf{u} _{\max}$
BGK	1.0	1.0	0.0	5.75×10^{-5}
MRT	1.0	1.0	0.0	5.46×10^{-5}
BGK	1.0	0.6	-0.7	8.15×10^{-5}
MRT	1.0	0.6	-0.7	6.77×10^{-5}
BGK	0.501	1.0	0.0	2.28×10^{-3}
MRT	0.501	1.0	0.0	9.97×10^{-5}
BGK	0.501	1.0	-0.9	1.43×10^{-3}
MRT	0.501	1.0	-0.9	7.03×10^{-5}
BGK	1.0	0.501	-1.0	9.49×10^{-4}
MRT	1.0	0.501	-1.0	1.85×10^{-4}
BGK	1.0	0.501	0.7	2.01×10^{-3}
MRT	1.0	0.501	0.7	2.09×10^{-4}
BGK	1.0	0.501	0.9	1.42×10^{-3}
MRT	1.0	0.501	0.9	1.75×10^{-4}

viscosity is regarded as gas [31]. The schematic illustrations of the above two cases are shown in Fig. 4(a) and (b), respectively.

For the first validation, as shown in Fig. 4(a), the computational domain is 80×160 . The upper and lower boundaries are the inlet and outlet boundaries, respectively. Initially the red fluid (non-wetting fluid) is put in the upper section of the domain and does not enter the tubes. The widths of the left and right tubes are $r_L = 24$ l.u. and $r_R = 32$ l.u., respectively. In our simulations, $\theta^{eq} = 45^\circ$. The contact angle is set through the scheme mentioned in Section 3.3. Hence the corresponding capillary pressures for the left and right tubes are

$$P_{cl} = \frac{2\sigma \cos \theta^{eq}}{r_L} = 1.59 \times 10^{-5}, \quad P_{cr} = \frac{2\sigma \cos \theta^{eq}}{r_R} = 1.19 \times 10^{-5}, \quad (21)$$

respectively. The other important parameters in our simulations are $A = 10^{-4}$, $\beta = 0.5$, $\tau_r = 0.51$, $\tau_b = 1.5$. That means the kinematic viscosity ratio between the non-wetting and wetting fluid is $\frac{\tau_r - 0.5}{\tau_b - 0.5} = \frac{1}{100}$. According to Table 1, the surface tension in these simulations is $\sigma = 2.7 \times 10^{-4}$.

From Fig. 5(a), we can see that for the smallest pressure difference between the inlet and outlet, $\Delta P = 1.0 \times 10^{-5} < P_{cr}$, the non-wetting fluid is not able to enter into either tube even t is large enough. In Fig. 5(b), when $P_{cr} < \Delta P < P_{cl}$, the non-wetting fluid enters into the wider tube (the right one) but it is unable to percolate into the narrower tube. In Fig. 5(c), when $\Delta P = 3.3 \times 10^{-5}$, which is larger than P_{cl} , the non-wetting fluid would pass through both tubes. The result is very consistent with the basic principle of pore-network simulations.

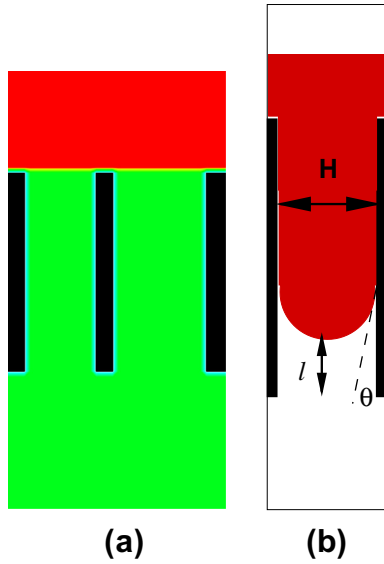


Fig. 4. (a) Injection of a non-wetting gas into two parallel capillary tubes, (b) liquid filling a capillary tube that initially contains gas. H is the width of the capillary tube and l is the length of the liquid column that has penetrated the capillary. The red and black are non-wetting component (gas) and the solid, respectively. (For interpretation of the references to color in this figure legend, the reader is referred to the web version of this article.)

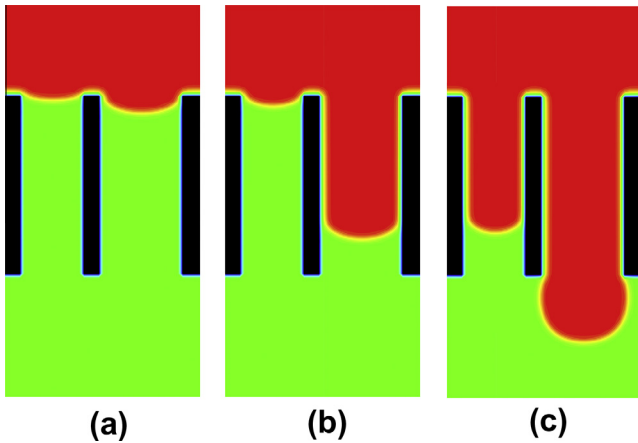


Fig. 5. Snapshots of the injection of a non-wetting fluid into two parallel capillary tubes with different ΔP , which is the pressure difference between the inlet and outlet. The widths of the left and right tubes are 24 l.u. and 32 l.u. respectively. (a) $\Delta P = 1.0 \times 10^{-5} < P_{cr}$, $t = 4 \times 10^6$ t.s., (b) $\Delta P = 1.4 \times 10^{-5}$, i.e., $P_{cr} < \Delta P < P_{cl}$, $t = 3.6 \times 10^6$ t.s., (c) $\Delta P = 3.3 \times 10^{-5} > P_{cl}$, $t = 10^6$ t.s. The black, red and green represent the solid, the non-wetting and wetting fluid respectively, $\theta^{eq} = 45^\circ$. (For interpretation of the references to color in this figure legend, the reader is referred to the web version of this article.)

For the simulations of capillary filling dynamic, the computational domain is 12×400 , as shown in Fig. 4(b), the left and right boundaries in the middle of the computational domain are solid nodes. The periodic boundary condition is applied on both the upper and lower boundaries, as well as on the upper and lower left and right boundaries without solid nodes. In the simulation, $\tau_r = 0.51$, $\tau_b = 1.5$, the kinematic viscosities of the gas (non-wetting component) and liquid are $\nu_G = c_s^2(\tau_r - 0.5)\delta t = \frac{0.01}{3}$, and $\nu_L = \frac{1}{3}$. The dynamic viscosity ratio is $\frac{\nu_r}{\nu_G} = 100$, which is sufficiently high that viscous dissipation in the gas phase can be ignored [31]. Ignoring the viscous dissipation is a basic assumption in the derivation of the following analytical solution Eq. (22). Here the gas (red component) is non-wetting and the equilibrium contact angle

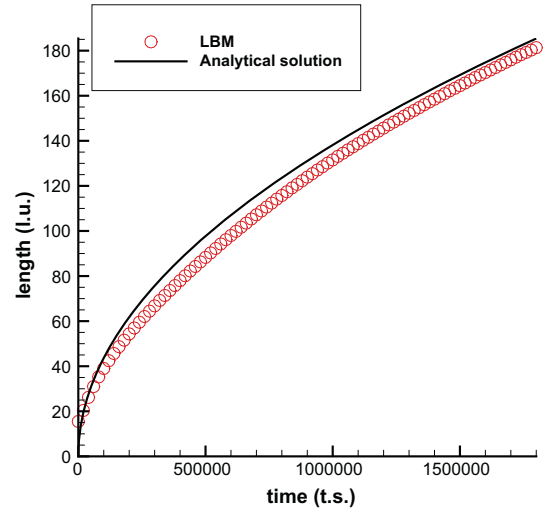


Fig. 6. The the length of the liquid column (l.u.) that has penetrated the capillary as a function of time, the initial penetration is about 15 l.u. at $t = 0$.

is set to be $\theta = 45^\circ$. In the simulation, $A = 10^{-3}$, and $\sigma = 2.7 \times 10^{-3}$, width of the capillary tube $H = 10$ l.u. The analytical solution for the length of tube filled with liquid l as a function of time is [31]

$$l = \left(\frac{\sigma H \cos \theta}{3 \rho \nu_L} \right)^{\frac{1}{2}} \sqrt{t}, \quad (22)$$

where $\rho = 1$ m.u./l.u.².

According to the parameters in our simulation, the analytical solution is $l = \sqrt{0.01909} \sqrt{t}$. From Fig. 6, it is seen the our numerical simulation is very consistent with the analytical solution.

5. Immiscible displacements in porous media

In the study of Lenormand et al. [27], it was found that in porous media, the capillary number and dynamic viscosity ratio are the two most important factors that affect the displacement behaviors. Generally speaking, there are three typical displacement patterns: capillary fingering, viscous fingering, and stable displacement [27]. For stable displacement, the front between the two fluids is almost flat with some irregularities at the scale of a few pores. Very little of the displaced fluid is trapped behind the front. For viscous fingering, tree-like fingers spread across the whole porous medium and present no loops [27]. For capillary fingering, “the fingers grow in all directions, even backward (toward the entrance)” [27]. The displaced fluid may be trapped due to the loops developed by the fingers. The size of the trapped cluster varies from the pore size to the whole porous medium [27].

In our simulations, the porous medium is generated by placing circles with different radii in a 900 l.u. \times 900 l.u. domain. Any two circles are not allowed to overlap and the minimum gap between any two circles is set to be 4 l.u. The radii of the randomly distributed circles range from 24 l.u. to 5 l.u. The porosity of the domain is 0.661 and the intrinsic permeability of the porous medium is 15.3 l.u.², which is determined by single-phase lattice Boltzmann simulations. The left and right sides of the domain are periodic. In the displacement simulations, the domain was originally occupied by the wetting fluid (‘blue’ component, which is white in figures, $\rho_b = 1.0$ m.u./l.u.³; for the ‘red’ component, which is the minority component, $\rho_r = 10^{-8}$ m.u./l.u.³). The wetting fluid is displaced vertically by the non-wetting fluid (red in figure, contact angle = 180° and $\rho_r = 1.0$ m.u./l.u.³, for the minority component

Table 3
Numerical stability comparison between the BGK and MRT R–K models.

Case	u_i	A	$\log(Ca)$	τ_r	τ_b	BGK applicable?	MRT applicable?
a	$1 \cdot e-2$	$1 \cdot e-2$	-2.92	1.5	0.51	No	Yes
b	$1 \cdot e-2$	$1 \cdot e-3$	-1.92	1.5	0.51	No	Yes

$\rho_b = 10^{-8}$ m.u./l.u.³). In our study, the densities of the two fluids in the solid nodes are set to be $\rho_{wr} = 0.0$ and $\rho_{wb} = 1.0$ m.u./l.u.³.

Our simulations are run until ‘breakthrough’ occurs, which means the injected fluid reaches the lower boundary. The non-wetting saturations (S_{nw}) are measured when breakthrough occurs. From the above definitions of the three patterns, we can see that S_{nw} of stable displacement is the highest and S_{nw} for viscous fingering is the lowest.

The capillary number is defined as $Ca = \frac{\rho_{nw} \gamma_{nw} u_i}{\sigma}$, where ρ_{nw} is the initial density of the non-wetting component and u_i is the inlet velocity of non-wetting component with unit ‘l.u./t.s’.

We investigated the numerical stability of our simulations. Two cases with low capillary number were simulated using both the MRT and BGK R–K models. Table 3 shows that the two cases which can be simulated using the MRT R–K model are not stable with the BGK R–K model. In the following MRT studies we also find a similar situation, i.e., some cases that can be simulated by the MRT model are not applicable using the BGK model. Hence, the MRT model has better numerical stability than the BGK model.

Seventeen cases with different viscosity ratios and capillary numbers are simulated and the parameters are shown in Table 4. The non-wetting saturations (S_{nw}) are listed in the last column. Fig. 7 shows flow pattern transitions from stable displacement to capillary fingering when M is fixed to be 500. When the capillary number is large ($\log(Ca) = 2.08$, case 7), the flow pattern is stable displacement and it has a large non-wetting saturation ($S_{nw} \approx 0.83$). When $\log(Ca) = -1.92$, the flow pattern becomes capillary fingering and $S_{nw} = 0.721$ (case 13). Fig. 7(b) shows an intermediate case and the non-wetting saturation is about 0.78.

From Fig. 8(a) we can see that for case 2 with $\log M = 0$ and an intermediate Ca , the displacement pattern is viscous fingering. When M is fixed and Ca increases to $\log(Ca) = 2.79$ (Fig. 8(b)), the flow pattern does not change. When both M and Ca decrease, the flow pattern still remains unchanged but the fingers become thicker and S_{nw} slightly decreases. Here we can see in this flow pattern, S_{nw} approximately ranges from 0.31 to 0.46 in Fig. 8(a)–(c).

According to the flow patterns, the seventeen cases illustrated in Table 4 are classified into three groups. The first six cases are viscous fingering, which approximately have a saturation $S_{nw} \in [0.31, 0.46]$. The 7th case to the 12th case are stable displacement,

Table 4
Cases with different viscosity ratio M and capillary number Ca .

Case	u_i	A	$\log(Ca)$	τ_b	τ_r	$\log(M)$	Saturation (S_{nw})
1	$1 \cdot e-2$	$1 \cdot e-6$	2.79	1	1	0	0.433
2	$5 \cdot e-3$	$1 \cdot e-3$	-0.51	1	1	0	0.451
3	$5 \cdot e-4$	$5 \cdot e-3$	-2.21	1	1	0	0.461
4	$1 \cdot e-2$	$1 \cdot e-3$	-1.92	1.5	0.51	-2	0.310
5	$1 \cdot e-2$	$1 \cdot e-2$	-2.92	1.5	0.51	-2	0.321
6	$1 \cdot e-3$	$1 \cdot e-2$	-2.92	1.5	0.6	-1	0.330
7	$1 \cdot e-3$	$1 \cdot e-6$	2.08	0.502	1.5	2.7	0.862
8	$1 \cdot e-3$	$1 \cdot e-5$	1.08	0.502	1.5	2.7	0.862
9	$1 \cdot e-3$	$1 \cdot e-4$	0.08	0.502	1.5	2.7	0.832
10	$5 \cdot e-3$	$1 \cdot e-6$	2.78	0.55	1.5	1.3	0.815
11	$1 \cdot e-2$	$1 \cdot e-3$	0.08	0.55	1.5	1.3	0.813
12	$2.5e-3$	$1 \cdot e-3$	-0.519	0.52	1.5	1.7	0.833
13	$5 \cdot e-4$	$5 \cdot e-3$	-1.92	0.502	1.5	2.7	0.721
14	$5 \cdot e-4$	$5 \cdot e-3$	-1.92	0.51	1.5	2	0.680
15	$5 \cdot e-4$	$5 \cdot e-3$	-1.92	0.6	1.5	1	0.677
16	$6 \cdot e-4$	$2 \cdot e-2$	-2.44	0.51	1.5	2	0.637
17	$6 \cdot e-4$	$2 \cdot e-2$	-2.44	0.8	1.5	0.5	0.563

which have the highest saturations $S_{nw} \approx 0.83$ among the three patterns. The last five cases are capillary fingering with $S_{nw} \in [0.56, 0.72]$. From Table 4, we can see that the saturations in each group are slightly different. In the following discussion, the saturation inside each group is regarded as ‘constant’.

Fig. 9 shows pattern distributions in the M – Ca plane. The above three groups roughly form three domains and cases in each domain have similar flow patterns. The boundaries that separate the domains are approximately drawn and are represented by the thick gray dashed lines. Our phase-diagram for the 900×900 porous medium is consistent with that obtained through experiments [27]. The general shape of the boundaries of the three domains is almost the same as that illustrated in Ref. [27]. The difference between our results and those of Ref. [27] is some translation of the boundaries of the domains. This translation might be attributed to differences in pore size distributions [27] and the overall size of the porous medium between our simulations and the results in Ref. [27].

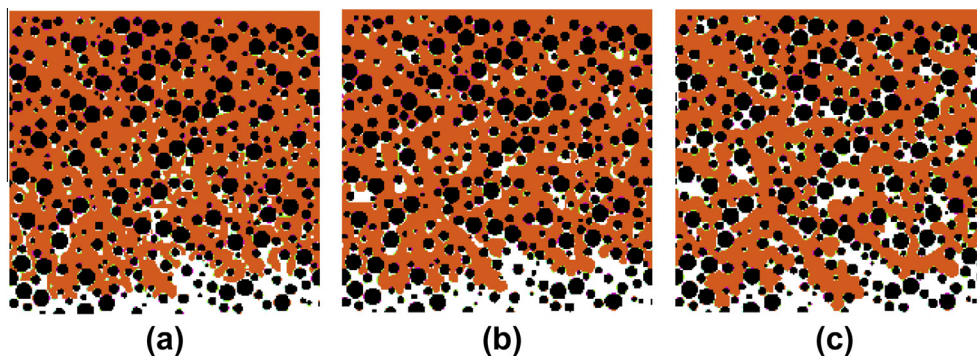


Fig. 7. From stable displacement to capillary fingering ($M = 500$). (a) case 7 ($\log(Ca) = 2.08$), (b) a case of $u_i = 5 \cdot 10^{-4}$, $A = 10^{-3}$, $\log(Ca) = -1.217$, $\tau_1 = 0.502$, $\tau_2 = 1.5$, (c) case 13 ($\log(Ca) = -1.92$). The red and black represent the non-wetting fluid and solid, respectively. The white area is occupied by wetting fluid. (For interpretation of the references to color in this figure legend, the reader is referred to the web version of this article.)

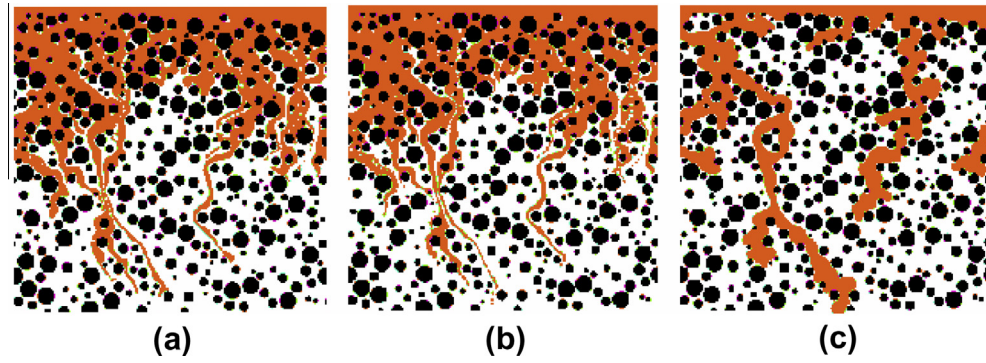


Fig. 8. Viscous fingering obtained from typical combination of different M and Ca , (a) case 2 ($M = 1, \log(Ca) = -0.51$), (b) case 1 ($M = 1, \log(Ca) = 2.79$), (c) case 6 ($M = -1, \log(Ca) = -2.92$). The red and black represent the non-wetting fluid and solid, respectively. The white area is occupied by wetting fluid. (For interpretation of the references to color in this figure legend, the reader is referred to the web version of this article.)

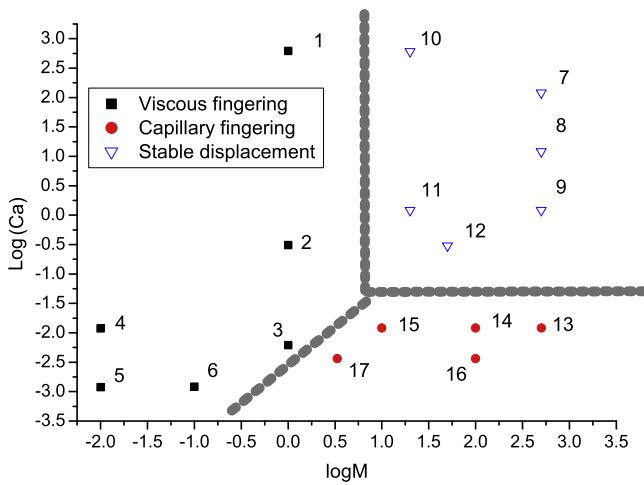


Fig. 9. Plot of the constant-saturation domains for the simulations of the 900×900 porous medium with different viscosity ratios and capillary numbers. The thick gray dashed lines represent the boundaries approximately drawn to separate the three domains.

6. Conclusion

In this paper, pressure and velocity boundary conditions for single phase flow are extended to simulate multiphase flows. The boundary condition is not only limited to the R–K model, it is also applicable to the other popular multiphase lattice Boltzmann models. The MRT R–K model presented is applied to study two-phase flow in porous media. Two advantages of the MRT R–K model are demonstrated. One is the significantly reduced spurious current, and the other is better numerical stability. With these advantages, two-component flows in porous media with both Ca and M ranging from 10^{-3} to 10^3 are simulated. All three typical flow patterns are reproduced and three domains in the M – Ca phase-diagram are obtained. The boundaries that separate the three domains are qualitatively consistent with the experimental study presented in Ref. [27].

Acknowledgements

This work was supported by the National Science Foundation of China (NSFC, Grant No. 10802085).

Appendix A

The transformation matrix M for 2D is [26]:

$$\begin{pmatrix} 1 & 1 & 1 & 1 & 1 & 1 & 1 & 1 & 1 \\ -4 & -1 & -1 & -1 & -1 & 2 & 2 & 2 & 2 \\ 4 & -2 & -2 & -2 & -2 & 1 & 1 & 1 & 1 \\ 0 & 1 & 0 & -1 & 0 & 1 & -1 & -1 & 1 \\ 0 & -2 & 0 & 2 & 0 & 1 & -1 & -1 & 1 \\ 0 & 0 & 1 & 0 & -1 & 1 & 1 & -1 & -1 \\ 0 & 0 & -2 & 0 & 2 & 1 & 1 & -1 & -1 \\ 0 & 1 & -1 & 1 & -1 & 0 & 0 & 0 & 0 \\ 0 & 0 & 0 & 0 & 0 & 1 & -1 & 1 & -1 \end{pmatrix}$$

References

- [1] Scardovelli R, Zaleski S. Direct numerical simulation of free-surface and interfacial flow. *Annu Rev Fluid Mech* 1999;31:567–603.
- [2] Liu HH, Valocchi A, Kang QJ. Three-dimensional lattice Boltzmann model for immiscible two-phase flow simulations. *Phys Rev E* 2012;85:046309.
- [3] Angelopoulos AD, Paunov VN, Burganos VN, Payatakes AC. Lattice Boltzmann simulation of nonideal vapor-liquid flow in porous media. *Phys Rev E* 1998;573:3237–45.
- [4] Sukop MC, Thorne DT. *Lattice Boltzmann modeling: an introduction for geoscientists and engineers*. 1st ed. Heidelberg, Berlin, New York: Springer; 2006.
- [5] Langaas K, Papatzacos P. Numerical investigations of the steady state relative permeability of a simplified porous medium. *Trans Porous Media* 2001;45:241–66.
- [6] Pan C, Hilpert M, Miller CT. Lattice-Boltzmann simulation of two-phase flow in porous media. *Water Resour Res* 2004;40:W01501.
- [7] Chau JF, Or D. Linking drainage front morphology with gaseous diffusion in unsaturated porous media: a lattice Boltzmann study. *Phys Rev E* 2006;74:056304.
- [8] Huang H, Lu X-Y. Relative permeabilities and coupling effects in steady-state gas-liquid flow in porous media: a lattice Boltzmann study. *Phys. Fluids* 2009;21(9):092104.
- [9] Shan X, Chen H. Lattice Boltzmann model for simulating flows with multiple phases and components. *Phys Rev E* 1993;47(3): 1815–1819.
- [10] Swift MR, Orlandini E, Osborn WR, Yeomans JM. Lattice Boltzmann simulations of liquid-gas and binary fluid systems. *Phys Rev E* 1996;54(5):5041–52.
- [11] Rothman DH, Keller JM. Immiscible cellular-automaton fluids. *J Stat Phys* 1998;52(3/4):1119–27.
- [12] Huang H, Wang L, Lu X-Y. Evaluation of three lattice Boltzmann models for multiphase flows in porous media. *Comput Math Appl* 2011;61(12):3606–17.
- [13] Huang H, Krafczyk M, Lu X-Y. Forcing term in single-phase and Shan–Chen-type multiphase lattice Boltzmann models. *Phys Rev E* 2011;84:046710.
- [14] Gunstensen AK, Rothman DH, Zaleski S, Zanetti G. Lattice Boltzmann model of immiscible fluids. *Phys Rev A* 1991;43(8):4320–7.
- [15] Latva-Kokko M, Rothman DH. Static contact angle in lattice Boltzmann models of immiscible fluids. *Phys Rev E* 2005;72(4):046701.
- [16] Leclaire S, Reggio M, Trepanier J-Y. Numerical evaluation of two recoloring operators for an immiscible two-phase flow lattice Boltzmann model. *Appl Math Model* 2012;36:2237–52.
- [17] Latva-Kokko M, Rothman D. Scaling of dynamic contact angles in a lattice-Boltzmann model. *Phys Rev Lett* 2007;98:254503.
- [18] Reis T, Phillips TN. Lattice Boltzmann model for simulating immiscible two-phase flows. *J Phys A: Math Theor* 2007;40:4033–53.
- [19] Liu H, Valocchi AJ, Kang QJ, Werth C. Pore-scale simulations of gas displacing liquid in a homogeneous pore network using the lattice Boltzmann method. *Trans Porous Media* 2013;99(3):555–80.

- [20] Tölke J, Krafczyk M, Schulz M, Rank E. Lattice Boltzmann simulations of binary fluid flow through porous media. *Philos Trans A Math Phys Eng Sci* 2002;360(1792):535–45.
- [21] Dong B, Yan YY, Li W, Song Y. Lattice Boltzmann simulation of viscous fingering phenomenon of immiscible fluids displacement in a channel. *Comput Fluids* 2010;39(5):768–79.
- [22] Grunau D, Chen S, Eggert K. A lattice Boltzmann model for multiphase fluid flows. *Phys Fluids A: Fluid Dyn* 1993;5(10):2557–62.
- [23] Rannou G. Lattice-Boltzmann method and immiscible two-phase flow. Master's thesis. Georgia Institute of Technology; 2008.
- [24] Huang HB, Huang JJ, Lu XY, Sukop MC. On simulations of high-density ratio flows using color-gradient multiphase lattice Boltzmann models. *Int J Mod Phys C* 2013;24(4):1350021.
- [25] Leclaire S, Reggio M, Trepanier J-Y. Isotropic color gradient for simulating very high-density ratios with a two-phase flow lattice Boltzmann model. *Comput Fluids* 2011;48(1):98–112.
- [26] Lallemand P, Luo LS. Theory of the lattice Boltzmann method: dispersion, dissipation, isotropy, galilean invariance, and stability. *Phys Rev E* 2000;61:6546–62.
- [27] Lenormand R, Touboul E, Zarcone C. numerical models and experiments on immiscible displacements in porous media. *J Fluid Mech* 1988;189:165–87.
- [28] Huang H, Thorne DT, Schaap MG, Sukop MC. Proposed approximation for contact angles in Shan-and-Chen-type multicomponent multiphase lattice Boltzmann models. *Phys Rev E* 2007;76:066701.
- [29] Zou QS, He XY. On pressure and velocity boundary conditions for the lattice Boltzmann BGK model. *Phys Fluids* 1997;9:1591–8.
- [30] Hou SL, Shan XW, Zou QS, Doolen GD, Soll WE. Evaluation of two lattice Boltzmann models for multiphase flows. *J Comput Phys* 1997;138(2):695–713.
- [31] Pooley CM, Kusumaatmaja H, Yeomans JM. Modelling capillary filling dynamics using lattice Boltzmann simulations. *Eur Phys J Spec Top* 2009;171(1):63–71.